



Electron nuclear dynamics of proton collisions with DNA/RNA bases at $E_{\text{Lab}} = 80$ keV: A contribution to proton cancer therapy research



A.J. Privett, J.A. Morales*

Department of Chemistry and Biochemistry, Texas Tech University, P.O. Box 41061, Lubbock, TX 79409-1061, USA

ARTICLE INFO

Article history:

Received 26 March 2014

In final form 13 April 2014

Available online 24 April 2014

ABSTRACT

The reactions: $\text{H}^+ + \text{B}$, B = adenine, cytosine, thymine and uracil, at $E_{\text{Lab}} = 80$ keV, relevant in proton cancer therapy, are investigated with the simplest-level electron nuclear dynamics (SLEND) and SLEND/Kohn-Sham-density-functional-theory (SLEND/KSDFT) methods. These time-dependent, direct, and non-adiabatic methods utilize nuclear classical mechanics and electronic single-determinantal wavefunctions. Results from this study include snapshots of the simulated reactions depicting base-to-proton electron transfers, base-to-proton total electron-transfer probabilities from various reactants' initial conditions, and base-to-proton 1-electron-transfer total integral cross sections. The last properties are compared with results from the only available experiment on these systems and from three alternative theories.

© 2014 Elsevier B.V. All rights reserved.

1. Introduction

Proton cancer therapy (PCT) utilizes high-energy H^+ projectiles (from an initial energy of 200–430 MeV down to a thermal energy at the projectiles' capture in deep tissues) to kill cancerous cells [1–4]. In all types of radiation therapies (PCT, $^{12}\text{C}^{+6}$ therapy, x-ray therapy, etc.), healing ultimately results from the radiation damage to cellular DNA [1–4]. Due to their high rate of division and reduced ability to repair damaged DNA, cancerous cells are much more vulnerable to DNA attacks than normal cells and are killed at a higher rate under irradiation [1–4]. The highest DNA damage occurs where a maximum energy deposition from the radiation to the tissues takes place—the Bragg peak in a graph plotting the radiation dose vs. the projectile's travelled distance [1–4]. Unlike photons in x-ray therapy, H^+ projectiles display a sharp Bragg peak during the last millimeters of their travel into the body. Thus, by focusing the Bragg peak on a tumor, PCT can inflict maximum damage to a cancerous area with minimum damage to the surrounding healthy tissues.

In a PCT session, the H^+ projectiles mostly collide with water molecules since these comprise ~70% of the human cell mass. These collisions trigger various cascade reactions that generate secondary ions (e.g. $\text{H}^+ + \text{H}_2\text{O} \rightarrow 2\text{H}^+ + \text{OH}^-$), radicals (e.g. $\text{H}^+ + \text{H}_2\text{O} \rightarrow \text{H}^+ + \text{H} + \text{OH}$), solvated/scattered electrons (e.g. $\text{H}^+ + 2\text{H}_2\text{O} \rightarrow \text{H}^+ + \text{H}_2\text{O} + e_{(\text{aq})}^-$) and localized heating [1,4,5]. The products of these reactions can eventually reach the cellular DNA and cause various types of structural damage on it (e.g. DNA bases' fragmentation and deletion,

sugar-phosphate lesions, DNA single- and double-strand breaks, etc. [1,4]).

While the clinical use of PCT as an alternative to x-ray therapy is firmly established, a thorough understanding of how the previous PCT reactions ultimately cause DNA damage and cellular death is seriously lacking [1]. This situation has motivated a number of experimental [6–9] and theoretical studies [1,4,5,10–13] of some of the discussed PCT reactions in order to reveal the physicochemical basis of PCT. An important type of PCT reaction requiring elucidation includes the DNA damage reactions caused by H^+ collisions with cellular DNA. Therefore, some research groups have recently studied H^+ collisions with DNA/RNA bases in the Bragg-peak energy regime ($E_{\text{Lab}} \sim 100$ keV) [8,11,12]; these collision systems constitute tractable prototypes of actual H^+ collisions with bases bonded to cellular DNA. A high point in this research approach is the recent scattering-beam experiment by Tabet et al. [8] that reported for the first time absolute total integral cross sections (ICs) for the one-electron-transfer (1-ET) reactions: $\text{H}^+ + \text{B} \rightarrow \text{H} + \text{B}^+$, B = adenine, cytosine, thymine and uracil, at $E_{\text{Lab}} = 80$ keV, among other data (note that these 1-ET reactions are often called single electron capture reactions/processes in the physics literature [11,12]). The availability of these experimental ICs strongly stimulates their prediction and further characterization with theoretical methods. However, thus far, only two theoretical studies have been conducted for that purpose: a study by Lekadir et al. [11], which employed the classical trajectory Monte Carlo (CTMC) with classical-over-barrier (COB: CTMC-COB) criteria method, and another study by Champion et al. [12], which employed the continuum distorted wave (CDW) and continuum

* Corresponding author. Fax: +1 (806) 742 1289.

E-mail address: jorge.morales@ttu.edu (J.A. Morales).

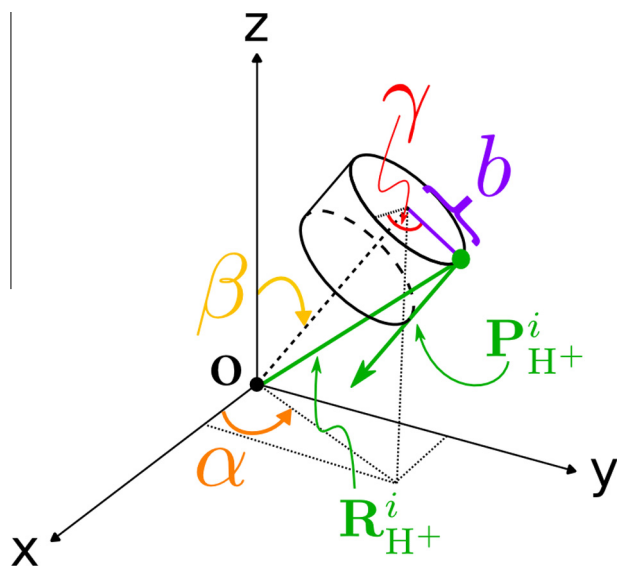


Figure 1. H^+ + DNA/RNA bases initial conditions. A given DNA/RNA base (not depicted for clarity's sake) is placed at rest with its center of mass at the origin of the coordinate axes and with the plane (uracil and thymine) or quasi-plane (remaining bases) of its heterocyclic ring(s) placed completely or with maximum coincidence on the x – y plane, respectively. The H^+ projectile is prepared with initial position and momentum $\mathbf{R}_{H^+}^i$ and $\mathbf{P}_{H^+}^i$, impact parameter b and relative orientation (α, β, γ) with Euler angles α , β and γ (cf. text for more details).

distorted wave-eikonal initial state (CDW-EIS) approximations. Overall, the calculated 1-ET total ICSSs from these two studies [11,12] compare satisfactorily with the experimental results [8], although all the calculated ICSSs appear underestimated with respect to their corresponding experimental values (cf. the discussion in Section 3).

The paucity of both experimental and theoretical 1-ET total ICSSs for the present systems makes the assessment of their corresponding accuracies difficult. Moreover, the previous theoretical studies [11,12] have shed no light on additional chemical details inaccessible by the experiment (cf. Figure 2). To remedy this situation, we decided to apply the electron nuclear dynamics (END) method at its simplest level (SL: SLEND) [14,15] to the present collision systems. END is a time-dependent, variational, direct and non-adiabatic approach for the simulation of chemical reactions at a wide range of collision energies [14,15]. END admits several realizations according to the level of sophistication conferred to its trial wavefunction [14,15] (e.g. multi-configuration [16] or coupled-cluster [17] wavefunctions for the electronic degrees of freedom). SLEND adopts classical mechanics and a single-determinantal wavefunction for the nuclear and electronic degrees of freedom, respectively [14,15]. These features make SLEND computationally suitable for simulating the present collision systems involving large DNA/RNA bases. Notably, in this investigation, besides the original SLEND method, which asymptotically corresponds to Hartree-Fock (HF) states, we employ our own SLEND/Kohn-Sham-density-functional-theory (SLEND/KSDFT) method [4,18]. SLEND/KSDFT incorporates time-dependent KSDFT concepts [19,20] into the SLEND framework to improve the electron correlation description of the original SLEND. The ability of SLEND and SLEND/KSDFT to correctly describe the present systems is attested by the good results obtained in previous SLEND and SLEND/KSDFT studies of related reactive systems at high collision energies [21–24] and of other PCT reactions (e.g. H^+ -induced fragmentations in DNA bases [4], H_2O [13,25,26] and aqueous clusters $(H_2O)_{2-4}$ [4,10]).

Below, we present our SLEND and SLEND/KSDFT study of H^+ + B, B = adenine, cytosine, thymine and uracil, at $E_{\text{Lab}} = 80$ keV in comparison with previous studies [8,11,12]. This investigation has been

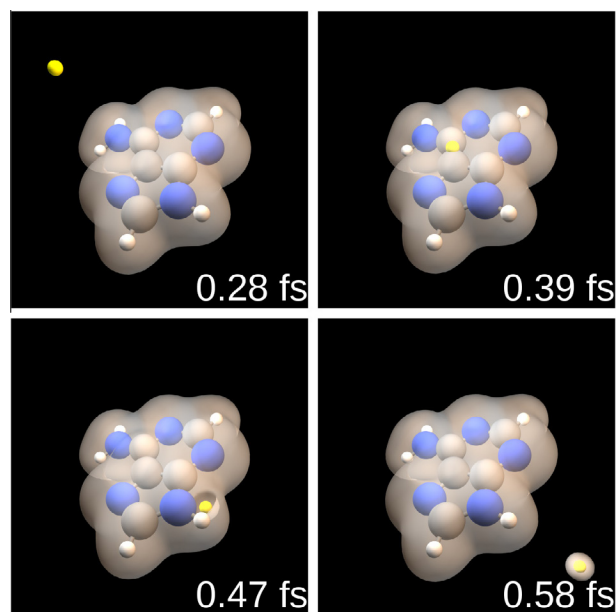


Figure 2. Snapshots of the SLEND/6-31G simulation of H^+ + adenine at $E_{\text{Lab}} = 80$ keV from projectile-target orientation $(301.72^\circ, 36.00^\circ, 301.72^\circ)$ and impact parameter $b = 0.0$ a.u. Time is given in femtoseconds. Travelling nuclei are represented by colored spheres (gray = C, blue = O, white = H initially belonging to adenine, and yellow = H initially belonging to the H^+ projectile) and the electron density by a selected gray isosurface. The outgoing projectile captures some electron density. (For interpretation of the references to color in this figure legend, the reader is referred to the web version of this article.)

made possible by our new parallel code PACE (Python Accelerated Coherent-states Electron-nuclear-dynamics, T. V. Grimes and J. A. Morales, Texas Tech University, 2010–2014; cf. Ref. [4], Section 4) and marks the largest chemical systems exhaustively studied with SLEND and SLEND/KSDFT to date.

2. Methods

2.1. SLEND and SLEND/KSDFT

Comprehensive discussions about SLEND [14,15,27], SLEND/KSDFT [4,18] and the END framework [4,14,15,27] can be found in the cited references. Therefore, we present herein a brief outline of those methods. END is a time-dependent, variational, direct and non-adiabatic approach to simulate chemical reactions [4,14,15]. A particular END realization adopts appropriate trial functions for the nuclear $|\Psi_N^{\text{END}}\rangle$ and electronic $|\Psi_e^{\text{END}}\rangle$ wavefunctions comprising the total wavefunction $|\Psi_{\text{Total}}^{\text{END}}\rangle = |\Psi_N^{\text{END}}\rangle |\Psi_e^{\text{END}}\rangle$; subsequently, the END dynamical equations are obtained by subjecting $|\Psi_{\text{Total}}^{\text{END}}\rangle$ to the time-dependent variational principle (TDVP) [28]. In SLEND, where $|\Psi_{\text{Total}}^{\text{SLEND}}\rangle = |\Psi_N^{\text{SLEND}}\rangle |\Psi_e^{\text{SLEND}}\rangle$, the nuclear wavefunction $|\Psi_N^{\text{SLEND}}\rangle$ for a system having N_N nucleus is the product of $3N_N$ frozen, narrow, Gaussian wave packets:

$$\langle \mathbf{X} | \Psi_N^{\text{SLEND}}(t) \rangle = \langle \mathbf{X} | \mathbf{R}(t), \mathbf{P}(t) \rangle = \prod_{A=1}^{3N_N} \exp \left\{ - \left[\frac{X_A - R_A(t)}{2\Delta R_A} \right]^2 + iP_A(t)[X_A - R_A(t)] \right\} \quad (1)$$

with average positions $\mathbf{R}_A(t)$, average momenta $\mathbf{P}_A(t)$ and widths $\{\Delta R_A\}$. While the END framework allows for a quantum treatment of the nuclei [14,15], SLEND adopts the zero-width limit for all

the nuclear wave packets in “open = “|” > $\Psi_N^{\text{SLEND}} : \Delta R_A \rightarrow 0 \quad \forall A$ prior to obtaining its dynamical equations. That procedure generates a classical nuclear dynamics as discussed in the following paragraph. The SLEND electronic wavefunction $|\Psi_e^{\text{SLEND}}\rangle$ for a system having N_e electrons is a complex-valued, spin-unrestricted, single-determinantal wavefunction in the Thouless representation [29]:

$$\langle \mathbf{x} | \Psi_e^{\text{SLEND}}(t) \rangle = \langle \mathbf{x} | \mathbf{z}(t), \mathbf{R}(t) \rangle = \det \{ \chi_h | \mathbf{x}_h; \mathbf{z}(t), \mathbf{R}(t) \}; \quad (2)$$

$$\chi_h = \phi_h + \sum_{p=N_e+1}^K z_{ph} \phi_p; 1 \leq h \leq N_e$$

where $K > N_e$ is the size of the electronic basis set and $\{\chi_h\}$ are non-orthogonal dynamical spin-orbitals (DSOs) [14,15]. The DSOs are linear combinations of orthogonal molecular spin-orbitals (MSOs) $\{\phi_h, \phi_p\}$ with complex-valued coefficients $\mathbf{z}(t) = \{z_{ph}(t)\}$; the MSOs are classified as occupied $\{\phi_h\}$ or unoccupied $\{\phi_p\}$ with respect to a reference single-determinantal state $|0\rangle = |\phi_1 \dots \phi_i \dots \phi_{N_e}\rangle$. The MSOs are constructed at initial time via a regular self-consistent-field (SCF) unrestricted HF (UHF) procedure involving K travelling atomic basis functions centered on the nuclear positions $\mathbf{R}_A(t)$. SLEND adopts the less frequently used Thouless single-determinantal wavefunction $|\Psi_e^{\text{SLEND}}\rangle = |\mathbf{z}, \mathbf{R}\rangle$ [29] because this preempts numerical instabilities in the SLEND dynamical equations (cf. Refs. [4,14] for full details).

The SLEND dynamical equations are obtained via the TDVP [28] applied to the trial function $|\Psi_{\text{Total}}^{\text{SLEND}}\rangle$ [4,14,15]. The SLEND TDVP procedure involves constructing the quantum Lagrangian $L_{\text{SLEND}} = \langle \Psi_{\text{Total}}^{\text{SLEND}} | i\partial/\partial t - \hat{H} | \Psi_{\text{Total}}^{\text{SLEND}} \rangle / \langle \Psi_{\text{Total}}^{\text{SLEND}} | \Psi_{\text{Total}}^{\text{SLEND}} \rangle$, applying the zero-width limit to all the nuclear wave packets in $|\Psi_{\text{Total}}^{\text{SLEND}}\rangle$, and imposing the stationary condition to the quantum action $A_{\text{SLEND}} : \delta A_{\text{SLEND}} = \delta \int_{t_1}^{t_2} L_{\text{SLEND}}(t) dt = 0$, with appropriate boundary conditions at the endpoints [4,14,15]. The described procedure generates the SLEND dynamical equations as a set of Euler-Lagrange equations: $d(\partial L_{\text{SLEND}}/\partial \dot{q}_i)/dt = \partial L_{\text{SLEND}}/\partial q_i$, for the SLEND variational parameters $\{q_i(t)\} = \{R_A(t), P_A(t), z_{ph}(t), z_{ph}^*(t)\}$. The resulting SLEND dynamical equations in matrix form are [4,14,15]:

$$\begin{bmatrix} i\mathbf{C} & \mathbf{0} & i\mathbf{C}_R & \mathbf{0} \\ \mathbf{0} & -i\mathbf{C}^* & -i\mathbf{C}_R^* & \mathbf{0} \\ i\mathbf{C}_R^\dagger & -i\mathbf{C}_R^\dagger & \mathbf{C}_{RR} & -\mathbf{I} \\ \mathbf{0} & \mathbf{0} & \mathbf{I} & \mathbf{0} \end{bmatrix} \begin{bmatrix} \frac{d\mathbf{z}}{dt} \\ \frac{d\mathbf{z}^*}{dt} \\ \frac{d\mathbf{R}}{dt} \\ \frac{d\mathbf{P}}{dt} \end{bmatrix} = \begin{bmatrix} \frac{\partial E_{\text{Total}}}{\partial \mathbf{z}} \\ \frac{\partial E_{\text{Total}}}{\partial \mathbf{z}^*} \\ \frac{\partial E_{\text{Total}}}{\partial \mathbf{R}} \\ \frac{\partial E_{\text{Total}}}{\partial \mathbf{P}} \end{bmatrix} \quad (3)$$

In Eq. (3), E_{Total} is the total energy:

$$E_{\text{Total}} = \sum_{A=1}^{N_N} \frac{\mathbf{P}_A^2}{2M_A} + \sum_{A,B>A}^{N_N, N_N} \frac{Z_A Z_B}{|\mathbf{R}_A - \mathbf{R}_B|} + T[\rho_1] + J[\rho] - K[\rho_1] + \int d\mathbf{r} v_{\text{ext}}[\mathbf{r}; \mathbf{R}(t)] \rho(\mathbf{r}) \quad (4)$$

where the first and the second terms are the kinetic and repulsion energies of the nuclei, respectively; $T[\rho_1]$, $J[\rho]$, and $K[\rho_1]$ are the kinetic, classical self-repulsion and exchange energies of the electrons, respectively [30]; $\rho_1 = \rho_1(\mathbf{r}, \mathbf{r}', t)$ and $\rho = \rho(\mathbf{r}, t)$ are the spinless one-electron density matrix [30] and one-electron density [30] of the evolving electronic wavefunction $|\Psi_e^{\text{SLEND}}(t)\rangle = |\mathbf{z}(t), \mathbf{R}(t)\rangle$, respectively; and $v_{\text{ext}}[\mathbf{r}; \mathbf{R}(t)] = -\sum_{A=1}^{N_N} Z_A |\mathbf{r} - \mathbf{R}_A(t)|^{-1}$ is the exter-

nal potential caused by the moving nuclei. In addition, \mathbf{C} , \mathbf{C}_R and \mathbf{C}_{RR} :

$$\begin{aligned} (\mathbf{C}_{XY})_{ik,jl} &= -2\text{Im} \left. \frac{\partial^2 \ln S}{\partial X_{ik} \partial Y_{jl}} \right|_{\mathbf{R}'=\mathbf{R}}; (\mathbf{C}_{X_{ik}})_{ph} = \left. \frac{\partial^2 \ln S}{\partial z_{ph}^* \partial X_{ik}} \right|_{\mathbf{R}'=\mathbf{R}}; \\ \mathbf{C}_{ph,qg} &= \left. \frac{\partial^2 \ln S}{\partial z_{ph}^* \partial z_{qg}} \right|_{\mathbf{R}'=\mathbf{R}}; \\ S &= \langle \mathbf{z}'(t), \mathbf{R}'(t) | \mathbf{z}(t), \mathbf{R}(t) \rangle \end{aligned} \quad (5)$$

are the dynamic metric matrices. \mathbf{C}_R and \mathbf{C}_{RR} can be seen as the SLEND non-adiabatic coupling terms, whose importance for the proper description of non-adiabatic effects is discussed in Ref. [31].

The formulation of the SLEND/KSDFT method [4,18] starts by considering Eqs. (3)–(5) as its fundamental dynamical equations and proceeds by reformulating their components along the lines of the time-dependent KSDFT [19,20]. The resulting SLEND/KSDFT dynamical equations look exactly the same as the SLEND ones, Eqs. (3)–(5), but with their components in a time-dependent KSDFT sense. Thus, the SLEND electronic wavefunction $|\Psi_e^{\text{SLEND}}\rangle = |\mathbf{z}, \mathbf{R}\rangle$, Eq. (2), is recast as a Kohn-Sham single-determinantal wavefunction $|\Phi_{KS}\rangle$ [19,20] in the Thouless representation, $|\Psi_e^{\text{SLEND/KSDFT}}\rangle = |\Phi_{KS}\rangle = |\mathbf{z}, \mathbf{R}\rangle$ [4,18], in terms of SCF unrestricted KSDFT (UKSDFT) MSOs $\{\phi_h^{\text{KSDFT}}, \phi_p^{\text{KSDFT}}\}$ [30]. The remaining components of the SLEND/KSDFT dynamical equations are expressed in terms of $|\Psi_e^{\text{SLEND/KSDFT}}\rangle = |\Phi_{KS}\rangle = |\mathbf{z}, \mathbf{R}\rangle$ or of its one-electron density $\rho(\mathbf{r}, t)$ as appropriate [4,18]. For instance, SLEND/KSDFT dynamic metric matrices \mathbf{C} , \mathbf{C}_R and \mathbf{C}_{RR} follow Eq. (4) but with $|\mathbf{z}, \mathbf{R}\rangle = |\Psi_e^{\text{SLEND/KSDFT}}\rangle = |\Phi_{KS}\rangle$, and the SLEND/KSDFT total energy E_{Total} is:

$$E_{\text{Total}} = \sum_{A=1}^{N_N} \frac{\mathbf{P}_A^2}{2M_A} + \sum_{A,B>A}^{N_N, N_N} \frac{Z_A Z_B}{|\mathbf{R}_A - \mathbf{R}_B|} + T_s[\rho] + J[\rho] + E_{xc}[\rho] + \int d\mathbf{r} v_{\text{ext}}[\mathbf{r}; \mathbf{R}(t)] \rho(\mathbf{r}) \quad (6)$$

where $T_s[\rho] = (-1/2) \sum_{i=1}^{N_{el}} \langle \mathbf{z}, \mathbf{R} | \nabla_i^2 | \mathbf{z}, \mathbf{R} \rangle / \langle \mathbf{z}, \mathbf{R} | \mathbf{z}, \mathbf{R} \rangle$ and $E_{xc}[\rho]$ are the KSDFT kinetic energy and exchange-correlation energy functionals [30] for the electrons, respectively (cf. Refs. [4,18] for further details about END/KSDFT).

2.2. Computational details, initial conditions and final state analysis

All the present simulations were computed with our own code PACE (Python Accelerated Coherent-states Electron-nuclear-dynamics, T. V. Grimes and J. A. Morales, Texas Tech University, 2010–2014; cf. Ref. [4], Section 4). PACE incorporates various advanced computer science techniques including a mixed programming language (Python for logic flow and FORTRAN/C++ for calculations), intra- and internode parallelization, and the OED/ERD atomic integral package [32] from the ACES III [33] code, *inter alia*.

The initial conditions for a pair of a DNA/RNA base target and a H^+ projectile for each individual simulation are schematized in Figure 1. The DNA/RNA base targets are prepared at rest in their equilibrium geometry and in their electronic ground state $|0\rangle$ at the UHF and UKSDFT levels for SLEND and SLEND/KSDFT simulations, respectively. The SCF UHF or UKSDFT MSOs in the reference $|0\rangle$ are localized with the Pipek–Mezey scheme [34] since localized MSOs decreased the computational cost of the dynamical simulations. The target's center of mass is placed at the origin of the laboratory-frame coordinate axes (cf. Figure 1). The plane (uracil and thymine) or quasi-plane (remaining bases) of the target's heterocyclic ring(s) is placed completely (uracil and thymine) or with maximum

coincidence (remaining bases) on the x - y plane of the aforesaid coordinate axes. The H^+ projectile is first prepared with position $\mathbf{R}_{H^+}^0 = (0, b \geq 0, -30 \text{ a.u.})$ and momentum $\mathbf{P}_{H^+}^0 = (0, 0, p_{H^+}^z > 0)$ where b is the projectile's impact parameter and $p_{H^+}^z$ corresponds to a kinetic energy $E_{\text{Lab}} = 80 \text{ keV}$. The definite initial conditions of the H^+ projectile $\mathbf{R}_{H^+}^i$ and $\mathbf{P}_{H^+}^i$ are obtained by rotating $\mathbf{R}_{H^+}^0$ and $\mathbf{P}_{H^+}^0$ by the Euler angles $0^\circ \leq \alpha < 360^\circ$, $0^\circ \leq \beta \leq 180^\circ$, and $0^\circ \leq \gamma < 360^\circ$ in the $z-y-z$ convention (cf. Figure 1); those operations define a relative projectile-target orientation denoted as (α, β, γ) . The selected values of the Euler angles are taken from a 60-point grid $\{(\alpha_1, \beta_1, \gamma_1), (\alpha_2, \beta_2, \gamma_2), \dots, (\alpha_{60}, \beta_{60}, \gamma_{60})\}$ developed in Ref. [35]; however, point-group symmetry considerations for the C_s -symmetry bases uracil and thymine permit the use of only 32 points in this grid for these two bases. This grid features a uniform sampling of the orientation space and provides a numerical quadrature scheme that ensures that integrals over the Euler angles (cf. Eq. (8)) remain invariant under several rotation operations (e.g. Wigner D-matrices correctly satisfy $\int_0^{2\pi} \int_0^\pi \int_0^{2\pi} D_{MM'}^J(\alpha, \beta, \gamma) \sin \beta d\alpha d\beta d\gamma = 0$ for $2 \leq J \leq 5$ under this scheme). For a given orientation (α, β, γ) , b is varied in adaptive steps $\Delta b = 0.5-1.0 \text{ a.u.}$ in the range $0 \leq b \leq b_{\text{Max}}$, where b_{Max} corresponds to the first asymptotic 1-ET probability lower than 0.01 (typically, $b_{\text{Max}} = 9.0-10.0 \text{ a.u.}$, cf. Figures 3–6). These initial conditions generate on average 806 single simulations per H^+ -DNA/RNA base pair. Each simulation ran for a total time of 40 a.u. (0.967 fs) rendering a final projectile-target separation $\geq 30 \text{ a.u.}$ At initial time, the SLEND or SLEND/KSDFT electronic Thouless single-determinantal wavefunction $|\Psi_e^{\text{SLEND}/(\text{KSDFT})}\rangle^i$ starts as a ground-state UHF or UKSDFT reference $|0\rangle$, $|\Psi_e^{\text{SLEND}/(\text{KSDFT})}\rangle^i = |\mathbf{z}^i = \mathbf{0}, \mathbf{R}^i\rangle = |0\rangle$ (cf. Eq. (2)). As time progresses, the system will access the non-adiabatic regime, where $|\Psi_e^{\text{SLEND}/(\text{KSDFT})}(t)\rangle = |\mathbf{z}(t), \mathbf{R}(t)\rangle$ with $\mathbf{z}(t) \neq \mathbf{0}$ will cease to resolve purely into the ground-state reference $|0\rangle$ (cf. Eq. (2)). At final time, the total probability for a base-to-proton n -ET: $H^+ + B \rightarrow H^{1-n} + B^{+n}$, $n \geq 0$, can be calculated with the auxiliary code RESOLVE in the PACE package. RESOLVE projects the final electronic wavefunction $|\Psi_e^{\text{SLEND}/(\text{KSDFT})}\rangle^f$ onto the UHF or UKSDFT states corresponding to the different ET channels [36]; that procedure

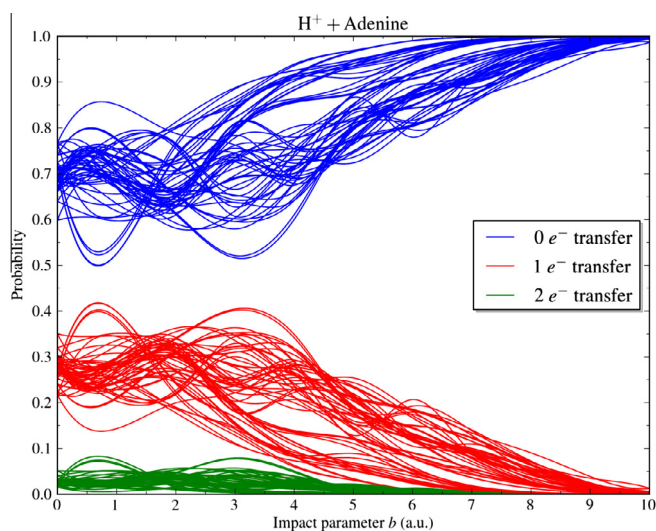


Figure 3. Base-to-proton 0-, 1- and 2-electron-transfer total probabilities vs. the projectile impact parameter b for H^+ + adenine at $E_{\text{Lab}} = 80 \text{ keV}$. The various curves per each type of electron transfer correspond to all the investigated projectile-target orientations (α, β, γ) .

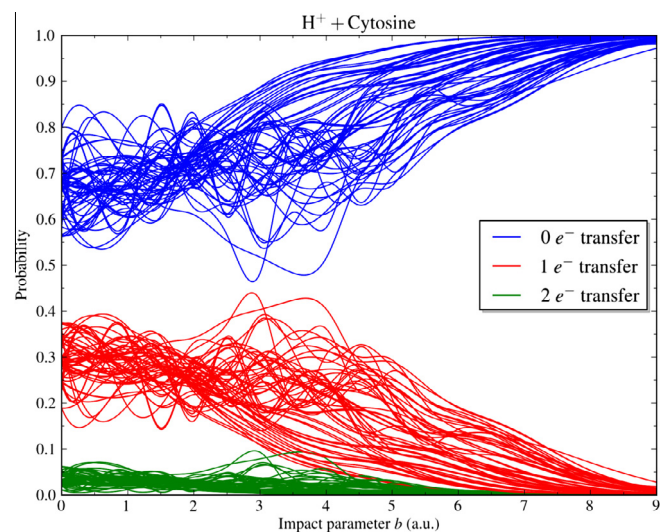


Figure 4. Base-to-proton 0-, 1- and 2-electron-transfer total probabilities vs. the projectile impact parameter b for H^+ + cytosine at $E_{\text{Lab}} = 80 \text{ keV}$. The various curves per each type of electron transfer correspond to all the investigated projectile-target orientations (α, β, γ) .

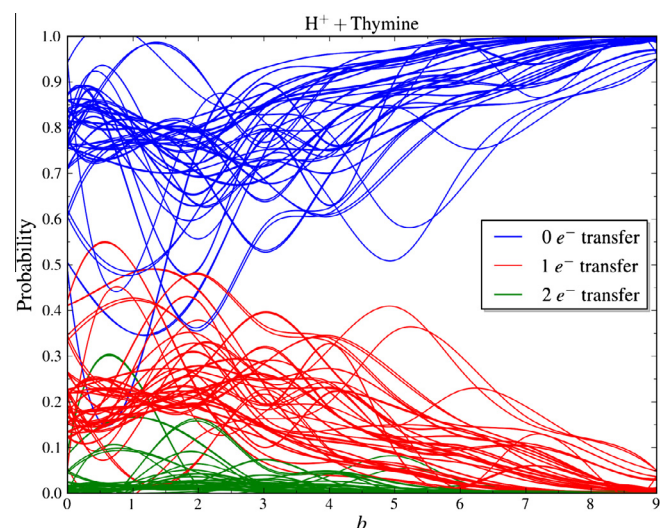


Figure 5. Base-to-proton 0-, 1- and 2-electron-transfer total probabilities vs. the projectile impact parameter b for H^+ + thymine at $E_{\text{Lab}} = 80 \text{ keV}$. The various curves per each type of electron transfer correspond to all the investigated projectile-target orientations (α, β, γ) .

requires generating all the excited determinants from the final-time ground-state reference $|0\rangle$, as those comprising a configuration-interaction expansion [36]. However, if one assumes on chemical grounds that n -ETs are negligible for $n > 2$ (e.g. for $H^+ + B \rightarrow H^{-2} + B^{+3}$, etc.), the relevant n -ET probabilities for $0 \leq n \leq 2$ can be calculated equivalently but far more feasibly from the final α and β Mulliken populations N_α and N_β of the outgoing projectile according to (P. M. McLaurin, PhD Dissertation, Texas Tech University, 2011):

$$\begin{aligned} P_{0\text{-ET}}(\alpha, \beta, \gamma, b) &= (1 - N_\alpha)(1 - N_\beta); \\ P_{1\text{-ET}}(\alpha, \beta, \gamma, b) &= N_\alpha(1 - N_\beta) + N_\beta(1 - N_\alpha); \\ P_{2\text{-ET}}(\alpha, \beta, \gamma, b) &= N_\alpha N_\beta \end{aligned} \quad (7)$$

From Eq. (7), the 1-ET total ICS $\sigma_{1\text{-ET}}$ is herein calculated as (P. M. McLaurin, *ibid.*):

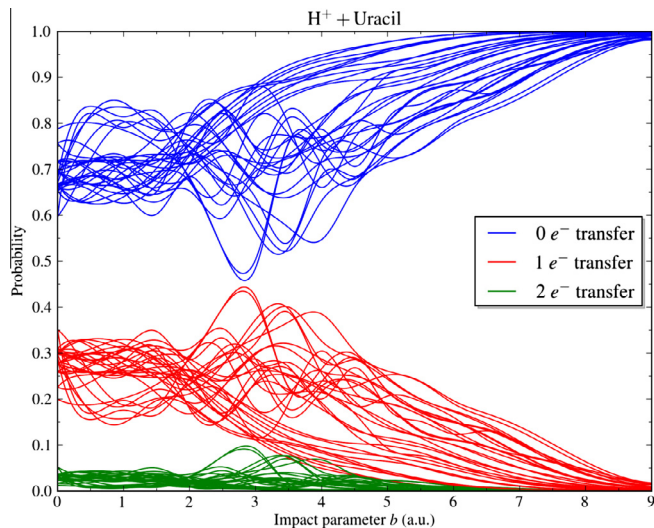


Figure 6. Base-to-proton 0-, 1- and 2-electron-transfer total probabilities vs. the projectile impact parameter b for H^+ + uracil at $E_{\text{Lab}} = 80$ keV. The various curves per each type of electron transfer correspond to all the investigated projectile-target orientations (α, β, γ) .

$$\sigma_{1\text{-ET}} = \frac{1}{4\pi} \int_0^{b_{\text{Max}}} \int_0^{2\pi} \int_0^{\pi} \int_0^{2\pi} b P_{1\text{-ET}}(\alpha, \beta, \gamma, b) db \times \sin \beta d\alpha d\beta d\gamma \quad (8)$$

where angular and impact-parameter integrations are performed by the quadrature scheme of Ref. [35] and cubic-spline integration, respectively. Notice that for atom-atom collisions involving spherical potentials, Eq. (8) reduces to the familiar ICS expression $\sigma_{1\text{-ET}} : P_{1\text{-ET}}(\alpha, \beta, \gamma, b) \rightarrow P_{1\text{-ET}}(b) \Rightarrow \sigma_{1\text{-ET}} = 2\pi \int_0^{b_{\text{Max}}} b P_{1\text{-ET}}(b) db$ [37].

3. Results and discussion

The main results of the current SLEND and SLEND/KSDFT simulations of H^+ + B, B = adenine, cytosine, thymine, and uracil, at $E_{\text{Lab}} = 80$ keV are presented herein. SLEND simulations employed the STO-3G, 3-21G, 6-31G and 6-31G/ H^{++**} basis sets. The mixed 6-31G/ H^{++**} basis set prescribes the 6-31++G** and 6-31G basis sets for the H nucleus of the initial H^+ projectile and the remaining nuclei, respectively, to probe the effect on the ET description by diffuse (++) and polarization (**) basis set functions added to the projectile's H nucleus. SLEND/KSDFT simulations employed the following combination of KSDFT functionals and basis sets: B3LYP/STO-3G, B3LYP/3-21G, BLYP/STO-3G, and PBE/STO-3G. In all cases, the size of the basis sets and/or the type of the KSDFT functionals have been determined by the high computational cost of these dynamical simulations involving large DNA/RNA bases. SLEND/KSDFT simulations are computationally more expensive than SLEND ones due to the former's inclusion of dynamical correlation effects.

Some illustrative results of the current simulations are presented in Figure 2. This figure shows four sequential snapshots of the SLEND/6-31G simulation of H^+ + adenine at $E_{\text{Lab}} = 80$ keV from the projectile-target orientation $(301.72^\circ, 36.00^\circ, 301.72^\circ)$ and impact parameter $b = 0.0$ a.u. that lead to a base-to-projectile ET. In that figure, time is given in femtoseconds. The travelling classical nuclei are represented by colored spheres and the evolving quantum electron density by a selected isosurface. The snapshots first show the H^+ projectile approaching the adenine target (0.28 fs) to collide with a point on one of the C–C bonds of the

adenine's ring system (0.39 fs); as a result of that violent collision, the projectile strongly deflects from its original trajectory (0.47 fs) and captures a noticeable electron density from the target (0.47 and 0.58 fs). This last feature clearly illustrates a base-to-projectile ET. The snapshots in Figure 2 demonstrate the capability of SLEND and SLEND/KSDFT to reveal important time-dependent details of a chemical reaction, something unattainable with time-independent scattering methods like the CDW and CDW-EIS approximations [12] (the time-dependent CTMC-COB method [11] might provide a depiction of its classical nuclear dynamics but not of the electronic one since electrons are not treated explicitly in that approach).

Figures 3–6 show the base-to-proton 0-ET (blue curves), 1-ET (red curves) and 2-ET (green curves) total probabilities: $P_{0\text{-ET}}(\alpha, \beta, \gamma, b)$, $P_{1\text{-ET}}(\alpha, \beta, \gamma, b)$, and $P_{2\text{-ET}}(\alpha, \beta, \gamma, b)$ (cf. Eq. (7)), at the SLEND/6-31G level from all the investigated orientations (α, β, γ) vs. the impact parameter b for H^+ + B $\rightarrow H^{+1/0/-1} + B^{0/+1/+2}$ at $E_{\text{Lab}} = 80$ keV with B = adenine (Figure 3), cytosine (Figure 4), thymine (Figure 5), and uracil (Figure 6). The various colored curves per each type of ET correspond to all the investigated orientations (α, β, γ) . Figures 3–6 reveal that with a few exceptions (most conspicuously, in the thymine case), the ET processes follow the trend: $P_{0\text{-ET}}(\alpha, \beta, \gamma, b) > P_{1\text{-ET}}(\alpha, \beta, \gamma, b) > P_{2\text{-ET}}(\alpha, \beta, \gamma, b) \forall (\alpha, \beta, \gamma)$ and b in all the investigated systems; clearly, the 0-ET channels predominate in these reactive systems. As expected on physical grounds, for all these systems, $P_{1\text{-ET}}(\alpha, \beta, \gamma, b)$ and $P_{2\text{-ET}}(\alpha, \beta, \gamma, b)$ values are significant at low ($0.0 \leq b \leq 2.0$ a.u.) and intermediate ($2.0 < b \leq 8.0$ a.u.) impact parameters, but they start to steadily decline to zero at large impact parameters ($b > 8.0$ a.u.); as $b \rightarrow \infty$, only 0-ET processes are predicted: $P_{0\text{-ET}}(\alpha, \beta, \gamma, b) \rightarrow 1$, due to negligible projectile-target interactions. As expected on chemical grounds, for all these systems, $P_{2\text{-ET}}(\alpha, \beta, \gamma, b)$ values remain very small $\forall (\alpha, \beta, \gamma)$ and b , a fact reflecting the low propensity of these systems toward the formation of unstable H^{-1} ions. The qualitative and quantitative properties of the n -ET total probabilities $P_{n\text{-ET}}(\alpha, \beta, \gamma, b)$, $0 \leq n \leq 2$, observed in Figures 3–6 in all the investigated systems at the SLEND/6-31G level are also observed with similar patterns in the same systems at the remaining SLEND and SLEND/KSDFT levels.

Finally, Table 1 lists the 1-ET total ICSs $\sigma_{1\text{-ET}}$ for H^+ + B $\rightarrow H + B^+$, B = adenine, cytosine, thymine, and uracil, at $E_{\text{Lab}} = 80$ keV from the only available experiment [8], the previous CDW[12], CDW-EIS[12], and CTMC-COB[11] theoretical investigations, and our SLEND and SLEND/KSDFT calculations with various basis sets and KSDFT functionals. On average, the absolute and relative percentage errors in the experimental ICSs $\sigma_{1\text{-ET}}^{\text{Expt.}}$ are $\epsilon^{\text{Expt.}} = 1.050 \times 10^{-19} \text{ m}^2$ and $\epsilon^{\text{Expt.}} 100/\sigma_{1\text{-ET}}^{\text{Expt.}} = 20.8\%$, respectively. On the other hand, on average, the absolute deviation from the experimental value $|\sigma_{1\text{-ET}}^{\text{Expt.}} - \sigma_{1\text{-ET}}^{\text{Theory}}| (10^{-19} \text{ m}^2)$ and the relative percentage deviation from the experimental value $|\sigma_{1\text{-ET}}^{\text{Expt.}} - \sigma_{1\text{-ET}}^{\text{Theory}}| 100/\sigma_{1\text{-ET}}^{\text{Expt.}}$ for the theoretical ICSs $\sigma_{1\text{-ET}}^{\text{Theory}}$ are: 2.98% and 52.0% (CDW), 4.55% and 87.5% (CDW-EIS), 4.05% and 75.8% (CTMC-COB), 4.11% and 77.1% (SLEND), and 4.46% and 77.6% (SLEND/KSDFT), respectively. Experimental errors and theoretical deviations are considerable as one might expect in dynamical and kinetic measurements and calculations, especially with the complex systems herein considered. Therefore, the performances of all the considered theoretical methods in predicting the experimental ICSs $\sigma_{1\text{-ET}}^{\text{Expt.}}$ can be deemed reasonable. Without exception, all the theoretical values from all the considered methods are smaller than their corresponding experimental values. With one exception, all the theoretical values lie outside the experimental error interval ('error bars'). The only exception is in the case of cytosine with the CDW approximation, where $\sigma_{1\text{-ET}}^{\text{CDW}} = 1.9 < \sigma_{1\text{-ET}}^{\text{Expt.}} = 2.3$ but $\sigma_{1\text{-ET}}^{\text{CDW}} = 1.9 > \sigma_{1\text{-ET}}^{\text{Expt.}} - \epsilon^{\text{Expt.}} = 2.3 - 0.5 = 1.8 (10^{-19} \text{ m}^2)$. Except for SLEND/KSDFT/STO-3G, all the theo-

Table 1

One-electron-transfer (1-ET) total integral cross sections (ICs) σ_{1-ET} for $H^+ + \text{DNA/RNA base} \rightarrow H + \text{DNA/RNA base}^+$ at $E_{\text{Lab}} = 80 \text{ keV}$ from experiment, from previous theories [theory A, continuum distorted wave (CDW) approximation; theory B, continuum distorted wave-eikonal initial state (CDW-EIS) approximation; and theory C, classical trajectory Monte Carlo with classical-over-barrier (CTMC-COB) criteria approach], and from SLEND and SLEND/KSDFT with various basis sets and KSDFT functionals. The mixed 6-31G/ H^{*++} basis set employs the 6-31+G** and 6-31G basis sets for the H nucleus in the initial H^+ projectile and the remaining nuclei, respectively.

1-ET Total ICs σ_{1-ET} for $H^+ + \text{DNA/RNA Bases}$ at $E_{\text{Lab}} = 80 \text{ keV}$ (10^{-19} m^2)													
Basis set Functional	Expt. [8]	Previous theories:			Current theories:				SLEND/KSDFT				
		A [12]	B [12]	C [11]	SLEND				SLEND/KSDFT				
					STO-3G	3-21G	6-31G	6-31G/ H^{*++}	STO-3G B3LYP	STO-3G BLYP	STO-3G PBE	3-21G B3LYP	
Adenine	5.8 ± 1.2	2.2	0.6	1.1	1.39	0.88	0.81	1.25	1.44				
Cytosine	2.3 ± 0.5	1.9	0.5	1.0	1.21	0.79	0.73	1.12	0.85				
Thymine	6.3 ± 1.3	2.3	0.6	1.1	1.33	0.82	0.68	1.14	1.15	1.37	1.36		
Uracil	6.0 ± 1.2	2.1	0.5	1.0	1.17	0.77	0.70	1.04	1.32	1.35	1.31	0.79	

retical methods predict ICs $\sigma_{1-ET}^{\text{Theory}}$ that scarcely differ in value along the four considered DNA/RNA bases. This uniformity is also observed in the experimental ICs $\sigma_{1-ET}^{\text{Expt.}}$ for adenine, thymine and uracil but not for cytosine, whose experimental ICs $\sigma_{1-ET}^{\text{Expt.}}$ is considerably lower than those of the remaining bases. Only SLEND/KSDFT/STO-3G shows a significant drop in the ICs $\sigma_{1-ET}^{\text{Theory}}$ value of cytosine with respect to those of the remaining bases. In SLEND and SLEND/KSDFT/B3LYP, the increase of the atomic basis set's size from minimal to double-zeta basis sets in the series: STO-3G, 3-21G, 6-31G, and STO-3G and 3-21G, respectively, leads to a decrease in the ICs $\sigma_{1-ET}^{\text{Theory}}$ values; however, in SLEND, the increase of the 6-31G atomic basis set with added diffuse and polarization functions to form the 6-31G/ H^{*++} basis set leads to an increase in the ICs $\sigma_{1-ET}^{\text{Theory}}$ value.

The present results establish the following ranking for the considered theoretical methods in their accuracy to predict the current experimental ICs: $\text{CDW} > \text{CTMC-COB} \approx \text{SLEND} \approx \text{SLEND/KSDFT} > \text{CDW-EIS}$. Then, at this point, it is appropriate to discuss the distinctive features of SLEND and SLEND/KSDFT [4,14,15,18] in comparison with the other three theoretical methods [11,12] to properly assess the performances of all these methods. The CTMC-COB approach uses a classical-mechanics model to describe both nuclei and electrons as whole particles, requires binding energies as parameters from previous quantum-mechanical calculations, and involves a set of *ad-hoc* criteria to model the electrons' ejections [11]. In contrast, SLEND and SLEND/KSDFT employ an *ab initio* quantum-mechanical description for the electrons that requires neither parameters from previous calculations nor *ad-hoc* criteria for the electronic dynamics [4,14,15,18]. The CDW and CDW-EIS approximations [12] use the CDW and CDW-EIS quantum scattering methods to describe electron processes and a HF description for the electrons in the DNA/RNA bases. However, the CDW and CDW-EIS approximations are employed by considering only one active electron at a time, with the remaining electrons forming a frozen core, and by assuming the complete neglect of differential overlap (CNDO) approximation [38] in the HF treatment during scattering [12]; in addition, in some calculations, the computed ionization energies of the occupied molecular orbitals were scaled so that their Koopman's ionization potentials match their experimental counterparts [12]. In contrast, SLEND and SLEND/KSDFT treat all the electrons as simultaneously active and do not assume any approximations and/or scaling in their related HF and KSDFT treatments [4,14,15,18]. Furthermore, as mentioned previously, the CDW and CDW-EIS approximations are time-independent [12], whereas SLEND and SLEND/KSDFT are time-dependent methods that can reveal the temporal evolution of chemical reactions (cf. Figure 2). Finally and perhaps most relevantly, the discussed CTMC-COB, CDW, and CDW-EIS methods [11,12] are

designed to *only* describe ionization processes including ET reactions. In contrast, SLEND and SLEND/KSDFT are versatile enough to describe those ionization processes as well as several others that occur simultaneously to the previous ones during chemical reactions (e.g. collision-induced rotational and vibrational excitations; fragmentation, rearrangement, substitution, and addition reactions, *inter alia*; cf. Ref. [4] for several examples of those excitations and reactions in various systems including $H^+ + \text{DNA bases}$ at $E_{\text{Lab}} = 1 \text{ keV}$). In summary, SLEND's and SLEND/KSDFT's reasonable performances in predicting the current ICs should be appraised in the context of those methods' capacities to predict various dynamical properties in diverse chemical reactions through the simultaneous treatment of nuclei and electrons without adjustable parameters and additional simplifying assumptions.

All the discussed theoretical ICs $\sigma_{1-ET}^{\text{Theory}}$ can be deemed reasonable in comparison with their experimental counterparts given the complexity of the investigated systems and the lack of alternative experimental results. However, the consistent discrepancy between predicted and measured ICs, where the former ones are always considerably lower than the latter ones, will require further experimental and theoretical investigations for its resolution.

4. Summary and conclusions

The SLEND [4,14,15] and SLEND/KSDFT [4,18] methods have been applied to $H^+ + B$, $B = \text{adenine, cytosine, thymine and uracil}$, at $E_{\text{Lab}} = 80 \text{ keV}$ for the first time. These collision systems are feasible prototypes for proton-induced DNA damage reactions in PCT. The employed methods are time-dependent, direct, and non-adiabatic and utilize nuclear classical mechanics and electronic single-determinantal wavefunctions. This investigation employing our parallel code PACE involves the largest molecular systems simulated with SLEND and SLEND/KSDFT to date. Present results with various atomic basis sets and KSDFT functionals include snapshots of the simulating reactions predicting base-to-proton ET, base-to-proton 0-, 1-, and 2-ET total probabilities from various reactants' initial conditions, and base-to-proton 1-ET total ICs. These last properties were carefully compared with results from the only experiment performed on these systems [8] and from three alternative theoretical methods: CDW[12], CDW-EIS[12], and CTMC-COB[11]. All considered theoretical 1-ET total ICs agree reasonably with their experimental counterparts exhibiting an accuracy performance ranking: $\text{CDW} > \text{CTMC-COB} \approx \text{SLEND} \approx \text{SLEND/KSDFT} > \text{CDW-EIS}$. However, unlike the other methods, SLEND and SLEND/KSDFT can also satisfactorily predict many other reactive processes occurring in this type of systems (cf. Ref. [4]) and reveal time-dependent dynamical details of both nuclei and electrons (cf. Figure 2). The five theoretical methods herein consid-

ered consistently predict 1-ET total ICSS lower in value than their experimental counterparts, a trend calling for additional experiments and calculations to resolve these discrepancies. Planned SLEND and SLEND/KSDFT studies will address these discrepancies and investigate additional PCT reactions.

Acknowledgments

The authors thank Professor Pablo Macri (Universidad Nacional de Mar del Plata, Argentina) for useful discussions about high-energy ET reactions. Present calculations were performed at the Texas Tech University Chemistry Computer Center (TTU CCC), the TTU High Performance Computer Center and the Texas Advanced Computing Center at the University of Texas at Austin. This material is based upon work partially supported by the National Science Foundation under grants CHE-0645374 (CAREER) and CHE-0840493 (TTU CCC).

References

- [1] A.V. Solov'yov, E. Surdutovich, E. Scifoni, I. Mishustin, W. Greiner, *Phys. Rev. E* 79 (2009) 011909.
- [2] M.A. Tabocchini, A. Campa, V. Dini, *Health Phys.* 103 (2012) 547.
- [3] E. Surdutovich, A.V. Solov'yov, *J. Phys.: Conf. Ser.* 438 (2013).
- [4] C. Stopera, T.V. Grimes, P.M. McLaurin, A. Privett, J.A. Morales, in: J.R. Sabin, E.J. Brandas (Eds.), *Advances in Quantum Chemistry*, vol. 66, Elsevier, 2013, p. 113. Chapter 3.
- [5] L. Pichl, M. Kimura, L. Yan, R.J. Buenker, *Trans. Nucl. Sci.* 51 (2004) 1407.
- [6] B. Boudaiffa, P. Cloutier, D. Hunting, M.A. Huels, L. Sanche, *Science* 287 (2000) 1658.
- [7] L. Sanche, *Nature* 461 (2009) 358.
- [8] J. Tabet et al., *Phys. Rev. A* 82 (2010) 022703.
- [9] A.N. Sidorov, T.M. Orlando, *J. Phys. Chem. Lett.* 4 (2013) 2328.
- [10] O. Quinet, E. Deumens, Y. Öhrn, *Int. J. Quantum Chem.* 109 (2008) 259.
- [11] H. Lekadir, I. Abbas, C. Champion, J. Hanssen, *Nucl. Instrum. Methods Phys. Res., Sect. B* 267 (2009) 1011.
- [12] C. Champion et al., *Phys. Med. Biol.* 57 (2012) 3039.
- [13] R. Cabrera-Trujillo, J.R. Sabin, E. Deumens, Y. Öhrn, *Oriental Effects in Energy Deposition by Protons in Water*, in: J.R. Sabin (Ed.), *Advances in Quantum Chemistry*, Academic Press, 2005, pp. 47–57. [http://dx.doi.org/10.1016/S0065-3276\(05\)48005-3](http://dx.doi.org/10.1016/S0065-3276(05)48005-3).
- [14] E. Deumens, A. Diz, R. Longo, Y. Öhrn, *Rev. Mod. Phys.* 66 (1994) 917.
- [15] E. Deumens, Y. Öhrn, *J. Phys. Chem. A* 105 (2001) 2660.
- [16] E. Deumens, Y. Öhrn, B. Weiner, *J. Math. Phys.* 32 (1991) 1166.
- [17] R.J. Bartlett, M. Musiał, *Rev. Mod. Phys.* 79 (2007) 291.
- [18] S.A. Perera, P.M. McLaurin, T.V. Grimes, J.A. Morales, *Chem. Phys. Lett.* 496 (2010) 188.
- [19] E. Runge, E.K.U. Gross, *Phys. Rev. Lett.* 52 (1984) 997.
- [20] M.A.L. Marques, E.K.U. Gross, *Annu. Rev. Phys. Chem.* 55 (2004) 427.
- [21] J.A. Morales, B. Maiti, Y. Yan, K. Tsereteli, J. Laraque, S. Addepalli, C. Myers, *Chem. Phys. Lett.* 414 (2005) 405.
- [22] C. Stopera, B. Maiti, T.V. Grimes, P.M. McLaurin, J.A. Morales, *J. Chem. Phys.* 134 (2011) 224308.
- [23] C. Stopera, B. Maiti, T.V. Grimes, P.M. McLaurin, J.A. Morales, *J. Chem. Phys.* 136 (2012) 054304.
- [24] C. Stopera, B. Maiti, J.A. Morales, *Chem. Phys. Lett.* 551 (2012) 42.
- [25] M. Hedström, J.A. Morales, E. Deumens, Y. Öhrn, *Chem. Phys. Lett.* 279 (1997) 241.
- [26] A. Blass, E. Deumens, Y. Öhrn, *J. Chem. Phys.* 115 (2001) 8366.
- [27] F. Hagelberg, *Electron Dynamics in Molecular Interactions Principles and Applications*, World Scientific, Singapore, 2014.
- [28] P. Kramer, M. Saraceno, *Geometry of the Time-Dependent Variational Principle in Quantum Mechanics*, Springer, New York, 1981.
- [29] D.J. Thouless, *Nucl. Phys.* 21 (1960) 225.
- [30] R.G. Parr, W. Yang, *Density-Functional Theory of Atoms and Molecules*, Oxford University Press, New York, 1989.
- [31] R. Longo, A. Diz, E. Deumens, Y. Öhrn, *Chem. Phys. Lett.* 220 (1994) 305.
- [32] N. Flocke, V. Lotrich, *J. Comput. Chem.* 29 (2008) 2722.
- [33] V. Lotrich, N. Flocke, M. Ponton, A.D. Yau, A. Perera, E. Deumens, R.J. Bartlett, *J. Chem. Phys.* 128 (2008) 194104.
- [34] J. Pipek, P.G. Mezey, *J. Chem. Phys.* 90 (1989) 4916.
- [35] S. Mamone, G. Pileio, M.H. Levitt, *Symmetry* 2 (2010) 1423.
- [36] J. Morales, A. Diz, E. Deumens, Y. Öhrn, *J. Chem. Phys.* 103 (1995) 9968.
- [37] M.S. Child, *Molecular Collision Theory*, Academic Press Inc, New York, 1974.
- [38] M.C. Zerner, in: K.B. Lipkowitz, D.B. Boyd (Eds.), *Reviews in Computational Chemistry II*, VCH Publishers Inc, 1991, p. 313.